USE OF OPTICAL SENSORS FOR ELECTRO-MECHANICAL ACTUATORS TORQUE ESTIMATION

Original
USE OF OPTICAL SENSORS FOR ELECTRO-MECHANICAL ACTUATORS TORQUE ESTIMATION / Aimasso, A., Berri, P.C., Bertone, M., Dalla Vedova, M.D.L.. - In: INTERNATIONAL JOURNAL OF MECHANICS AND CONTROL. - ISSN 1590-8844. - ELETTRONICO. - 25:2(2024), pp. 121-131. [10.69076/jomac.2024.0034]

Publisher:
Levrotto and Bella

Published
DOI:10.69076/jomac.2024.0034

ISSN 1590-8844
International Journal of Mechanics and Control, Vol. 25, No. 02, 2024
https://doi.org/10.69076/jomac.2024.0034

USE OF OPTICAL SENSORS FOR ELECTRO-MECHANICAL ACTUATORS TORQUE ESTIMATION

Alessandro Aimasso* Pier Carlo Berri* Matteo Bertone* Matteo D. L. Dalla Vedova*

* Department of Mechanical and Aerospace Engineering, Politecnico di Torino, Italy

ABSTRACT

The transition to extended electrical power feeds for subsystems in commercial aircraft has led to the adoption of new actuation systems for both primary and secondary flight controls. Electromechanical actuators (EMAs) are emerging as the most viable choice for these applications. Alongside this technological shift, there is a growing interest in developing innovative methods for monitoring the operational state and assessing the health of EMA systems during normal use. Currently, the evaluation of a system's condition relies on simulation models. For this study, the EMA system was validated using an experimental test bench designed to replicate the structure and operation of an electromechanical actuator. The primary focus of the work was on exploring new sensor technologies, specifically optical fiber-based sensors. These sensors' ability to measure the load applied to mechanical components was evaluated using the aforementioned experimental bench. A key challenge addressed was distinguishing the mechanical characteristics from the thermal effects in the sensor data. Both factors were present simultaneously, and their influence on the data analysis was not immediately clear due to experimental uncertainties and varying test conditions. The study aimed to develop methods for isolating these contributions, enabling more accurate monitoring of EMA system performance during operation.

Keywords: EMA, FBG, aerospace, safety, testing

1 INTRODUCTION

To fulfill the demands of the commercial aviation market while also meeting the increasingly narrow margins required by environmental rules, aircraft makers are continuously looking for innovative ways to boost the efficiency of the overall aircraft system. Over the years, significant development has been made in the propulsive, structural, and aerodynamic domains, resulting in technical saturation in terms of total aircraft configuration. As a result, the design work has centered on the creation of new aircraft systems and subsystems, with a particular emphasis on the methodology of energy absorption from the primary production source, represented by the engines. One of the best-known and most promising tactics used in aviation is the *More Electric* philosophy [1-3]. It entails designing airplanes whose systems are powered as much as feasible by electricity, typically by eliminating the pneumatic system and powering the air conditioning system's hydraulic pumps and compressors with electric motors. The main advantage of these solutions is that they boost the thermodynamic efficiency of the engine, which is no longer deducted with a portion of fluid from the compressor, allowing for more efficient power extraction [4-5]. Furthermore, the concentration of production and delivery into a single energy source simplifies and harmonizes various maintenance operations [6]. However, in order to supply the power demands of the connected equipment, this unique structure requires the existence of numerous power lines at different voltages. As a result, transformers and inverters must be installed to enable effective power transformation. Then it must examine the necessary redundancy and the potential of power crossing between the main generators and the other power lines. It is evident that the complexity of this enhanced electrical power distribution system (EPDS) for more electric aircraft (MEA) would increase, resulting in worse overall system reliability [7]. In particular, one of the most challenging

---

Contact author: Matteo Bertone**,** Matteo D.L. Dalla Vedova

[1]C.so Duca Degli Abruzzi 24, Torino (TO), 10129, Italy.
E-mail: matteo.bertone@polito.it , matteo.dallavedova@polito.it

aspects is represented by the need to use the so-called electromechanical actuators (EMA) in substitution to the electro-hydraulic ones, especially in the architecture of flight control system [8-10]. The classical configuration of this type of actuators is shown in Figure 1.

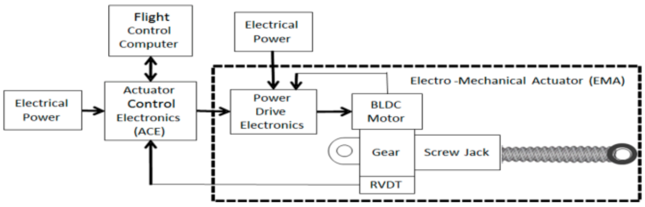

Figure 1 EMA scheme.

Inside the EMA, the electric motor is powered by power drive electronics, which regulate and/or transform the input electric power. The mechanical power generated by the motor is then transmitted to a gearbox, which converts torque and rotational speed into the quantities required for actuation. The presence of this component is required to install smaller and lighter electric motors. Finally, a recirculating ball system is installed downstream of the gearbox to change the motion from rotational to translational in order to move the flying surface. One of the most critical aspects related to EMA is their level of reliability and, more in general, their higher probability of failure. In this context, the development of prognostic and diagnostic algorithm and specifically thought monitoring systems are necessary to implement this technology onboard airplanes. In particular, the algorithms shall contain a lot of data arriving directly from senors integrated inside the system [11-14]. This work is therefore oriented to the validation of an innovative sensor network, based on optical fiber technology, monitoring the torque applied by the EMA’s motor. So, at first the experimental test bench, reproducing an EMA behaviour, is detailly described. Then, the sensors installation procedure is described, along with a description of their physical working principle. Finally, the test campaigns and the results are presented and discussed.

2 EMA TEST BENCH

To meet the study's objectives, the ASTRA research group at the Politecnico di Torino designed and developed an experimental test bench [15-17]. This bench simulates the behaviour of an EMA and it is made up of three primary modules: the *actuation module*, the *braking module*, and the *load module*. These modules are made up of many components, which are described in detail in the next chapters, while the overall structure of the test bench is depicted in the image below.

2.1 THE ACTUATION MODULE

The actuation module is made up of all the pieces that comprise the EMA system, as seen in Figure 2. The electric motor, as well as all of its power supply and control elements (PLC, CU, inverter), are part of a package known as the Sinamic S120 AC/AC Trainer Package, which is supplied by Siemens. The gearbox, position encoder, and voltage converter are not included in this package.

The *Programmable Logic Controller* (PLC) is the computer where command types and parameters can be configured. The computer then sends the command information to the control unit, which controls the electric motor activities. While the command is running on the system, various information on the operating status of the Siemens package is returned, which is kept by the computer for use as data in the post-processing phases. The PLC contains a Windows Embedded operating system with the STARTER software loaded. This software's video interface allows you to establish commands, manage operating choices for the entire Siemens system, and display and save operational variables.

The *control unit* (CU) installed on the bench, identified in the Siemens package by the code CU310-2 PN, regulates the operation of the electric motor according to the command information passed by the PLC. To carry out this duty, the CU regulates the power supply to the three motor windings based on the rotor position. This position information is obtained from the motor's specialized encoder and transmitted to the CU via a DRIVE CliQ connection. It should be noted that the CU merely maintains powering information, leaving the duty of ensuring an adequate power supply to the inverter. The connection between CU and PLC, on the other hand, is made using an Ethernet cable, and the connection between CU and inverter is made directly between the two components using a connector built into their respective casings. The *inverter* sends electricity to the electric motor coils as instructed by the control unit. This component, identified by the name and code Blocksize PM240-2, has a three-phase 380 V power supply, resulting in a wholly dedicated power line in comparison to the rest of the test bench. The test bench's *electric motor* is the Simotics S 1FK7060-2AC71-1CG0. It's a permanent magnet synchronous motor (PMSM) from the Siemens package discussed before. In order to line the motor shaft with the gearbox input shaft, which also houses the chain drive sprocket for the braking module, this motor is integrated into the test bench using a steel support.

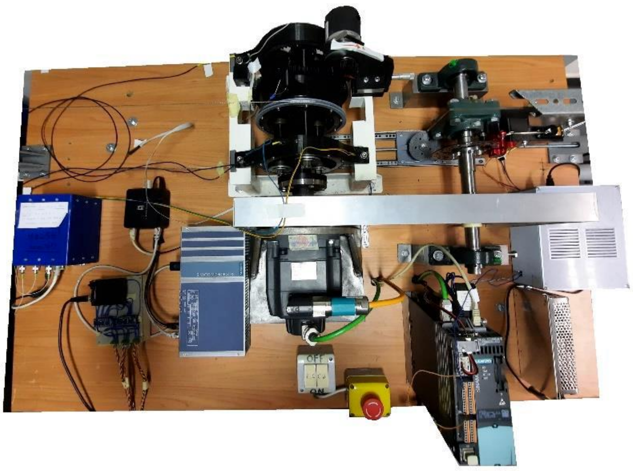

Figure 2 EMA test bench at Politecnico di Torino.

A flexible coupling is used to realize the coupling between the input gearbox shaft and the motor shaft. On the other side of the shaft output is a dedicated encoder that is part of the motor. Not to be mistaken with the function of the encoder mounted on the gearbox output shaft, which instead obtains the position data to close the control loop of the EMA, this encoder is required to transmit the rotor position to the CU in order to feed the motor coils in the proper manner.

A two-stage planetary *gearbox* with an overall gear ratio of 1:124 makes up the reduction gearbox that is mounted on the test bench. This part was created especially for the test bench mentioned and was made via 3D printing utilizing the fusion deposition modeling (FDM) technology. Because of the low mechanical properties of the plastic material, it is unable to apply significant torques, making this component the test bench's limiting factor. The steel frame supports the gearbox, which is positioned in line with the electric motor, and screws hold it in place at four spots.

As previously stated, the *encoder* on the test bench serves the purpose of closing the control loop by supplying the position signal of the gearbox output shaft. The Italsensor TSW581HS encoder model is the one that was fitted. It is an optical incremental encoder that is mounted on a gearbox structural appendage. A geared wheel outside the gearbox meshes with a pinion mounted on the position sensor's axis to guarantee the encoder's movement. A micro-mover that slides the sensor support along a guide can be used to experiment with the backlash play between the two gears.

A *converter* is necessary to convert the 220 V AC main power source to the 24 V DC power supply for the PLC and CU. Additionally, a second converter for the disc brake servomotor, which needs 6 V DC, also requires a 24 V DC power source.

2.2 THE BRAKING MODULE

The integration of a braking module into the test bench aims to introduce an additional braking torque on the electric motor shaft, allowing it to serve as a variable for system analysis. This braking torque holds dual significance. At first, it simulates the degradation of mechanical components within the actuator. Second, it facilitates operational and experimental purposes by providing a clearer characterization of the torque gain of the electric motor in the collected data. Without this braking torque, the gearbox alone would not generate sufficient torque to establish a meaningful correlation with the currents flowing through the electric motor. The braking module comprises three primary components, which are described in detail below.

The braking module is mounted on a shaft parallel to the one housing the motor and gearbox, requiring a transmission system to mechanically link the two modules. A motion drive is installed between the motor and the gearbox, where a sprocket is connected to the shaft. A roller chain engaged with this sprocket transfers motion to the parallel shaft, which houses the disc brake and a second sprocket. The two sprockets differ in tooth count, with the motor shaft sprocket having 34 teeth and the brake shaft sprocket having 23 teeth. This creates a gear ratio of 1.48, resulting in a faster rotation of the brake module shaft. For safety, the transmission system is enclosed within a plexiglass cover during test bench operations. The braking action is achieved by clamping two brake pads onto a brake disc using a mechanical caliper. This caliper is actuated by a small rod pulled by an electric servomotor controlled by a logic program loaded on an Arduino board. The caliper and servomotor are mounted on a 3D-printed plastic support attached to a metal plate. This plate is free to rotate around the shaft, thanks to two bearings. At the opposite end of the plate, a 3D-printed interface element secures it to the test bench and ensures mechanical continuity with a load cell positioned on the bench surface. In this configuration, when the brake is activated, all braking forces are transmitted to the load cell, enabling the calculation of the braking torque applied to the shaft based on the known arm length. To regulate the braking torque during operations, the servomotor's movements are managed by an Arduino R3 board programmed as a PI controller. By closing the control loop using force data from the load cell, the system ensures the desired braking torque is maintained, even as the shaft’s speed and direction fluctuate over time. Simultaneously, the loaded software logs the load cell data for use in post-processing analysis. Any actuator system, regardless of its application, is inevitably subjected to external loads. In the case of electromechanical actuators (EMA) used in aeronautical applications, these loads primarily arise from aerodynamic forces acting on the controlled surface.

2.3 THE LOAD MODULE

The *load module* is designed to simulate the external forces acting downstream of the EMA system. The core components of the load module consist of two steel coil springs located in the lower section of the test bench, enclosed within protective PVC tubes. These springs, characterized by an elastic constant K of 0.0615 N/m, generate a load proportional to the displacement applied by the control. One end of each spring is pulled via a cable connected to the gearbox output shaft, while the other end is anchored to load cells fixed to a stationary base. A system of *polymer cables* routed through a series of pulleys transfers the load generated by the springs. Although the springs create two separate forces, they are combined into a single torque load applied to the gearbox. This is achieved by winding the two cables, in opposite directions, onto a reel mounted on the gearbox output shaft. The pulleys and supports used to guide the cables along the desired path were fabricated using 3D printing and mounted on aluminum profiles securely attached to the test bench. The torque applied to the gearbox is measured indirectly through the *load cells* installed at the stationary ends of the springs. The torque value is calculated by multiplying the measured force by the arm length of the spool where the cables are wound. Data acquisition for this process is handled by the Arduino board, ensuring that all measurements are centralized in a single data collection system.

3 OPTICAL FIBER AND SENSORS INSTALLATION

Optical fiber sensors represent an emerging technology that is gaining traction in the sensor industry, particularly within the aerospace sector. These sensors are especially valuable in complex systems where traditional electrical sensors fail to meet performance requirements [18-20]. They are capable of measuring various physical and chemical properties of the materials on which they are installed. The working principle of optical fiber sensors is based on the transmission of light within the fiber. External physical or chemical disturbances can alter the light's propagation compared to nominal conditions, resulting in a measurable change detected by the sensor [21-22]. Compared to conventional sensors, optical fiber sensors offer several key advantages:

- Immunity to electromagnetic interference;
- The impossibility of conducting electricity;
- The possibility of being deployed in hostile environments;
- The significantly reduced volume and weight;
- The possibility of detection in normally inaccessible places
- The ease of remote control and the possibility of integrating several sensors on the same optical fiber
- The possibility of use in chemical processes and biomedical instrumentation
- High sensitivity and accuracy during detection
- The dual function of transducer and information transport channel, being realized with standard optical fibers and, therefore, compatible with existing optical fiber systems.

The use of fiber optics also brings disadvantages:

- They must be installed with high bending radius to avoid signal loss or accidental breakage;
- Installation can be very expensive as it requires a team of experts;
- Optical fibers are very delicate, requiring protection against mechanical stress.

In particular, in this work Bragg Grating sensors are used. They are generated using a UV laser, so producing a modulation according to the exposure pattern in the refractive index in the innermost layer of the fiber. The Fiber Bragg Grating will act as a filter by selecting specific wavelengths. The electromagnetic wave travelling within the core will be partially reflected at the refractive index changes. The maximum reflection will occur at the Bragg wavelength λB, which can be derived from the *fundamental Bragg equation*.

$$\lambda_B = 2 * n_{eff}\Lambda \tag{1}$$

This relationship connects the effective refractive index n_{eff} with the fringe period Λ. Light rays constructively interfere only for wavelengths corresponding to the grating pitch and a specific refractive index. Consequently, any change in the physical or chemical properties of the grating will result in a shift in the Bragg wavelength. The sensor filters out wavelengths far from the Bragg wavelength, allowing only those close to the Bragg wavelength to be reflected back to the receiver. As illustrated in the figure below, a variation in the grating spacing causes a shift in the reflected wavelength. This property enables the placement of multiple FBGs along the same optical fiber, each tuned to a unique Bragg wavelength and separated by sufficient distance. The maximum number of FBGs that can be installed on a single fiber is limited by the bandwidth of the laser emitted by the acquisition system. Moreover, the sensor's precision increases with the acquisition system's ability to accurately determine the Bragg wavelength of each FBG. The aim of this work is to monitor the torque supplied by the actuator motor using FBG. Considering the entire structure of the experimental bench, therefore, it was decided to instrument the external surface of the gearbox using optical fiber, which is so minimally invasive. In this way, considering the operating principle of an FBG, we want to associate the deformation induced on the gearbox with the copy that generated it. The gearbox's top and vertical views are depicted in the following picture, and the locations of the FBG sensors within the optical fiber are indicated in red. Installation locations were not picked at random.

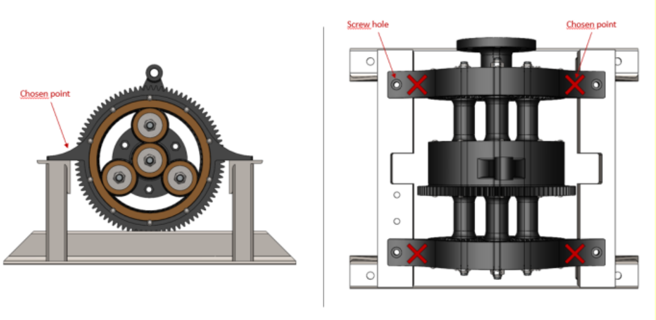

Figure 3 FBG sensors placement on gearbox.

These four symmetrical points were selected because they correspond to the locations where the binding reactions caused by the torque generated by the springs are transferred to the support that secures the gearbox. Consequently, these points experience the highest forces and deformations. At the same time, it is crucial to avoid placing the FBG Bragg grating too close to the screw, as the screw hole could interfere with the deformations measured by the sensor, potentially compromising the results. A second rationale for choosing these installation points is tied to the geometry of the selected locations. Fibers are typically mounted on flat surfaces that facilitate easier installation and provide an optimal operating environment, as they function only under tension. In this case, however, the fibers were intentionally installed on a concave surface to evaluate their performance, particularly their behavior under compression rather than solely under tension. The downside of this approach is that conventional installation procedures cannot be used. Instead, a method specifically tailored to the gearbox geometry was implemented. The fiber, as supplied by the manufacturer, is too fragile for direct use. To address this, it was reinforced with a heat-shrink covering, which does not enclose the entire optical fiber but only the section extending from the connector to the beginning of the gearbox support. This reinforcement improves the fiber’s mechanical strength and ease of handling, protecting the exposed section from accidental damage. The standard installation procedure involves attaching the optical fiber at one end to the specimen, typically a flat or similar surface. The fiber is pre-tensioned using a linear mover, ensuring it does not operate under compression. Pre-tensioning ensures that any applied compression simply reduces the existing tension, allowing the fiber to operate solely in a tensile field. However, due to the complex surface geometry of the gearbox, a mover cannot be used to apply tension. The fiber would likely detach from the surface if tensioned. To resolve this issue, a negative mold of the concave surface was designed using SolidWorks and fabricated with the fused deposition modeling (FDM) technique. The negative features a curvature matching the convex surface of the gearbox and includes a hole for the screw used to secure the gearbox to its support during fiber installation. Additionally, it has a triangular structure to facilitate gripping by the operator and ensure proper pressure application. The underside of the negative contains channels for fiber placement, minimizing shear stresses, which are the most critical and could lead to fiber failure.

The custom procedure for mounting optical fibers with a Bragg grating on the gearbox of an electromechanical servomechanism comprises the following nine steps:

1. Cleaning the installation surface
2. Sensor function check
3. Fixing optical fibre ends
4. Preparation of negative
5. Pretensioning the optical fibre
6. Tension evaluation
7. Glue arrangement
8. Pressure application
9. Removing the negative

4 TEST CAMPAIGN

Considering that the sensors are installed on a mechanical gear under torque stress, it is really interesting to investigate the possibility to directly correlate the wavelength variation to the torque variation without applying intermediate calculations on the punctual strain of the gearbox. The determination of the mechanical torque characteristic is therefore taken as the main objective of the study.

$$Kq = Wavelength\ [nm]\ Torque\ [Nm] \quad (2)$$

This coefficient is specific to the gearbox and the FBG sensor system under consideration. Any modifications to the geometry, material, installation method of the FBGs, or the sensors' locations would alter the overall mechanical properties of the system, leading to a different torque coefficient. To precisely characterize the Kq coefficient, it is essential to accurately determine the torque applied to the gearbox. For simplicity and rapid reconfiguration, supports were installed on the two cable branches where calibrated weights were placed. These supports were positioned along the vertical section of the cable, just after the first pulley. This setup ensures an accurate torque value applied to the gearbox, as the force on each cable branch directly corresponds to the weight placed on the supports. To ensure that only torque was applied, both branches were loaded with identical weights during the tests. In the initial testing phase, static tests were conducted with incremental loads to sequentially record wavelength and torque data. For this first experimental iteration, the equipment managing the EMA bench operation and fiber acquisition was used concurrently. Although the tests were static in nature and no active commands were executed, the bench control system remained operational throughout the tests. This ensured that the output shaft stayed fixed and compensated for the gearbox material's elastic deformations. The bench control system was managed via a computer running STARTER software, which did not perform any data

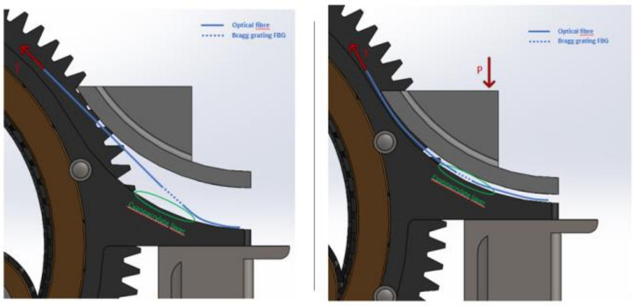

Figure 4 FBG bonding process.

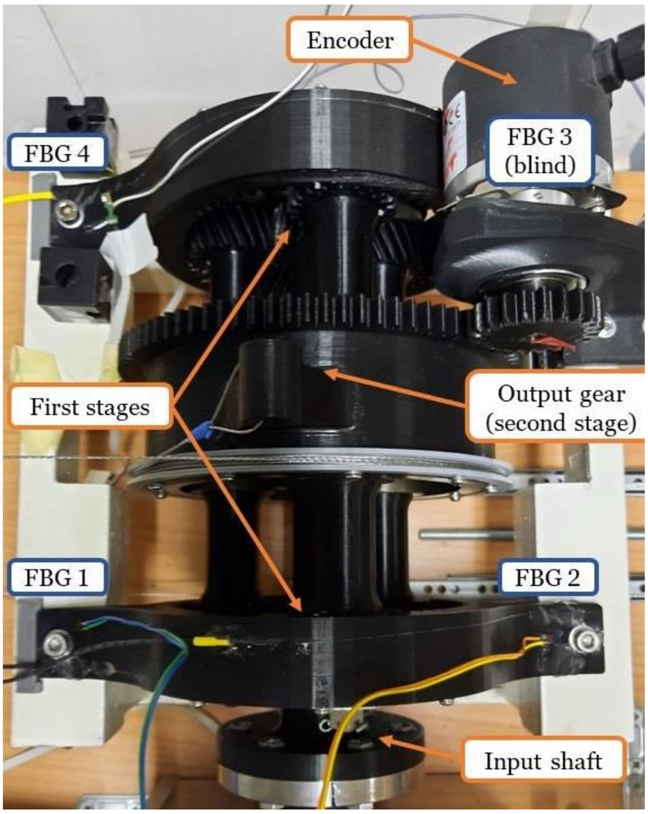

Figure 5 Gearbox with optical sensors.

acquisition from the Siemens equipment. Additionally, since the tests were entirely static, the braking module was left inactive throughout the tests. The data acquisition process for this initial set of experimental tests involved the following three fundamental steps:

- Manual application of weight and tightening of supports.
- Release of applied weight and stabilisation of any oscillations.
- Acquisition of wavelength data.

As there was no interest in detecting transient phenomena, the duration of the acquisition was rather short for a duration of four seconds. The data obtained was then averaged in order to derive a single value. The three-point procedure previously described was repeated for each applied weight. In total, eleven equally spaced load steps were used. Table 1 shows the weight values used for each individual test with the relative torque value calculated knowing that the radius of the winding spool is 0.1605 metres. These eleven trials were then repeated for four measurement cycles. In the first three, an increasing weight sequence was followed from test 0 to test 10, while in the last one, the reverse order was followed.

Table I - Experimental values

Test (#)	Weight (Kg)	Torque (Nm)
0	0	0
1	1.020	0.8031
2	2.029	1.5973
3	3.049	2.4004
4	4.030	3.1729
5	5.050	3.9759
6	6.031	4.7480
7	7.051	5.5511
8	8.043	6.3315
9	9.063	7.1346
10	10.084	7.9383

5 RESULTS AND DISCUSSION

The collected data are shown in figure xx. However, among the FBG sensors, only one was identified as a reliable data source. Channel three presented an excessively broad variability range, while channels one and two displayed behavior that appeared almost random relative to the loading sequence. The primary cause of this unreliable behavior was traced back to installation errors on these sensors. Additionally, the influence of the gearbox input shaft must be taken into account. Since FBG 1 and 2 are closest to this component, they are affected by the static reaction forces and torque exerted by the input shaft during position command control. Focusing on channel four, the wavelength growth generally corresponds to the increase in applied load across each measurement cycle. However, an unexpected wavelength shift was observed. Specifically, the wavelength displayed a displacement at the beginning of each measurement cycle compared to the previous one. Initially, this phenomenon was attributed to two main factors.

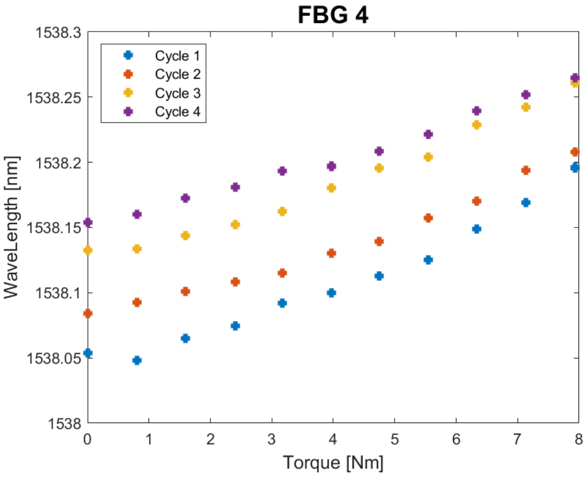

Figure 6 Example of FBG data.

- *Temperature change*: an increase or decrease in environmentak temperature generates respectively an expansion or contraction of the gearbox material. This phenomenon is reflected on the fiber where an additional wavelength term is added in addition to the term resulting from the applied torque.
- *Possible visco-plastic effects of the PLA*: the material of construction of the gearbox does not possess excellent mechanical properties. Therefore, the presence of visco-plastic effects has been hypothesised, resulting in a progressive increase in deformation, and therefore wavelength, as the load remains applied to the gearbox.

To remove the uncertainty linked to the first hypothesis, four additional measurement cycles were performed. The experimental setup was so modified: a SHT85 temperature - humidity probe was inserted to detect the laboratory environmental conditions. The acquisition of information from this sensor is done every ten seconds via an Arduino board connected to the same computer on which the fiber-optic acquisition software is installed. For these tests, it was decided to conduct the analysis without using the active position control system, instead simply locking the gearbox input shaft. This condition was introduced to eliminate any influence of the motor's torque on the gearbox's overall tension state. Consequently, it was unnecessary to operate the EMA test bench during these tests. However, the data quality for channels one and two remained insufficient to be considered reliable. In contrast, the data from FBG 3 showed significantly improved quality compared to previous tests, making this sensor's data valid for subsequent analysis processes. Maintaining the same graph format, the temperature trend corresponding to the wavelength acquisitions is also represented. The overall differences in wavelength trends between Figure 82 and Figure 80 are minimal. The correlation between torque increases and wavelength shifts, as well as the shift between cycles, is preserved in these tests. However, the temperature graph reveals a slight increase in laboratory temperature from the first to the fourth measurement cycle. Despite this, the temperature variation remains within a maximum absolute difference of 0.622°C across the measurements. Using the thermal constant from the literature [23], which is 0.01 [nm/°C], this variation does not justify an average wavelength difference of 0.0533 [nm] (e.g., maximum of 0.635 [nm] in test 2 and minimum of 0.366 [nm] in test 9).

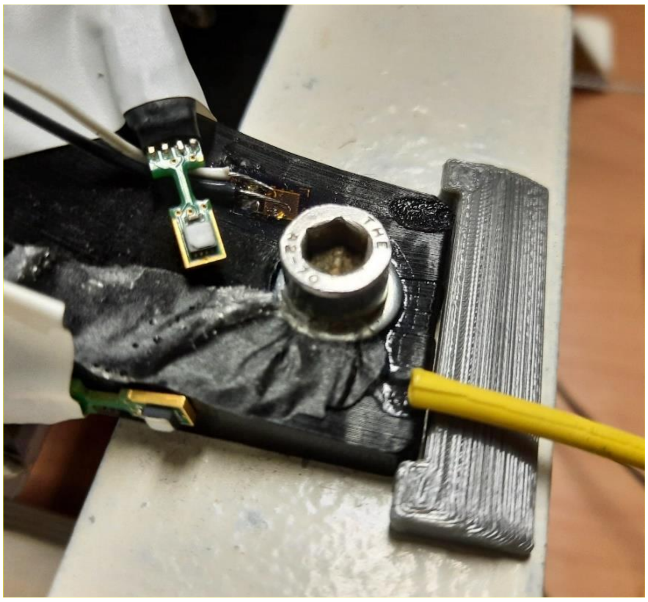
Figure 7 New FBG set up.

The second factor considered responsible for the consistent wavelength increase is the elastoplastic behavior of the PLA material used for the gearbox. To investigate this aspect, experimental tests were conducted using a different approach from prior tests. The weight values in Table 15 were used as reference, and for each test, the weight was alternately applied and removed, creating five load-unload cycles. A one-minute dwell time was maintained for each condition, with continuous wavelength acquisition throughout the test. These experiments aimed to identify evidence of repeatable wavelength or strain growth during the loading and unloading phases under the same applied weight. Such findings would suggest the presence of hysteresis in the fiber data, explaining the consistent wavelength increases observed during repeated loads in earlier tests.

Laboratory temperature data were also collected in parallel with these tests. The wavelength increase during individual tests was evident for loads of one, two, three, and five kilograms. However, for other tests, the phenomenon was less pronounced or even reversed, as seen in the six- and ten-kilogram tests, where a wavelength decrease occurred during loading phases. Overall, the repeatability of this behavior was inconsistent, providing weak evidence for material hysteresis under cyclic loading.

In the last two tests, a noticeable temperature decrease was observed. Similarly, the two- and five-kilogram tests exhibited temperature increases, which may explain the rise in fiber data values. This raises the possibility of a temperature correlation, questioning the validity of the thermal constant value from the literature (0.01 [nm/°C]) for this specific case study. It suggests that the actual thermal characteristic may be higher, with even slight temperature variations significantly impacting the wavelength in previous tests.

To derive the torque coefficient Kq, it is essential to isolate mechanical effects from thermal influences by correcting raw data for thermal variations. Given the high uncertainty surrounding the gearbox-sensors system's thermal characteristic, a preliminary calibration phase is necessary to quantify the actual thermal constant KT in the FBG installation zone.

A rigorous thermal calibration would typically require dismounting the gearbox from the test bench and performing tests in a climatic chamber. However, due to the challenges of disassembly, an alternative calibration strategy was adopted. This involved using metal blocks at different temperatures placed near the FBG sensor. Since channel four consistently provided reliable data in prior tests, the calibration focused on this sensor.

To create the setup, SHT85 temperature sensors were repositioned close to the fourth sensor. Aluminium blocks were mounted on either side of the connection between the steel frame and the gearbox support, providing a base for the metal plates used to adjust temperature. The plates were positioned near the FBG to minimize the distance and leverage thermal radiation and convection to alter the local temperature. To determine the KT coefficient, the same principle as for Kq was applied, but instead of relating torque to wavelength, the relationship was established between wavelength variation and temperature variation. Three thermal equilibrium points were chosen for calibration: one at -40°C for cold temperatures (using cooled plates), one at room temperature (achieved by removing the cold plates), and one at 90°C for high temperatures (using heated plates). Since the plates were not in direct contact with the gearbox, the gearbox never reached the extreme high or low temperatures, avoiding brittleness or melting of the PLA. Continuous acquisition of temperature and wavelength data was conducted throughout the test.


Figure 8 Thermal testing.

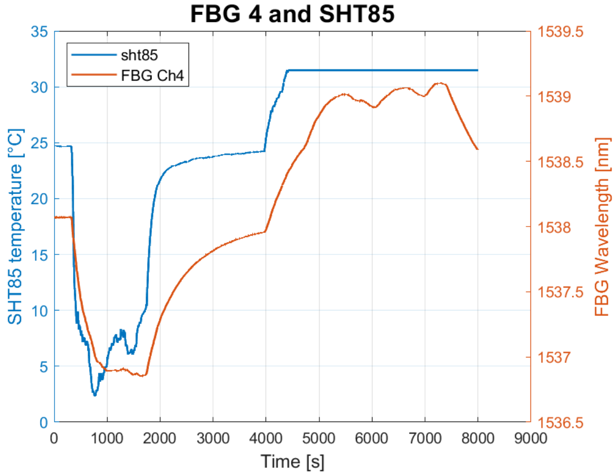

Figure 9 Thermal testing data.

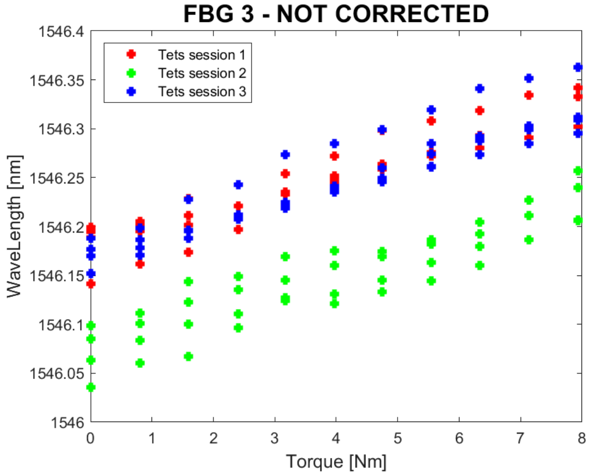

Figure 10 Data not corrected.

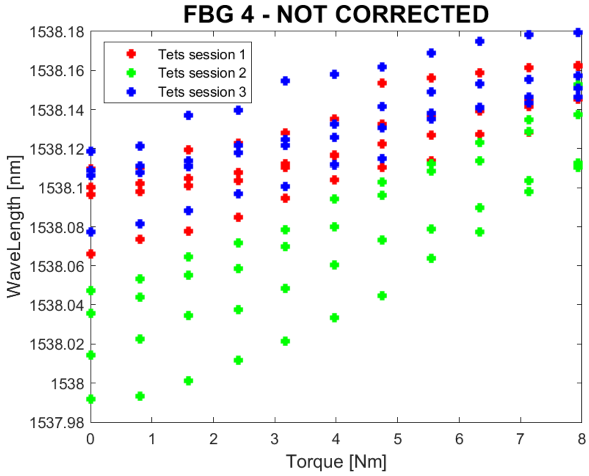

Figure 11 Data not corrected

Even during the cold phase, the results obtained were unsatisfactory. Although the wavelength value appeared to stabilize, the temperature data exhibited significant fluctuations in this phase. As a result, associating the wavelength value with a precise temperature value was not feasible. Nevertheless, it was possible to estimate the \(K_T \) coefficient using the start and end points of the heating transient towards room temperature. Assuming these two points represent thermal equilibrium due to the absence of heat flow from the plates, the angular coefficient of the resulting line was calculated. Using this newly determined value, which is significantly higher than the previously assumed one, corrections were applied to the data from earlier measurement cycles, excluding the first series, where temperature data had not yet been recorded. By convention, the wavelength data were adjusted to an equivalent 0°C condition:

$$\lambda i{-}corrected = \lambda i{-}test - Ti{-}test\ KT \qquad (3)$$

The necessity of temperature correction becomes evident as it significantly reduces data dispersion. Despite the experimental nature of the tests, some level of randomness in the data points was inevitable. However, after correction, the wavelength data dispersion decreased by approximately one-third compared to the original data shown in Figures 81 and 82. Additionally, this thermal correction proved effective for the third sensor, validating the use of the thermal coefficient derived earlier for both FBGs. To proceed with the interpolation phase and derive the torque coefficient, a larger dataset was required to improve statistical reliability. Simultaneously, having additional data allowed for verification of the temperature correction method. If the corrected values in the second dataset aligned with those from the first dataset, the validity of the correction method would be confirmed. The experimental method remained unchanged, including the number of measurement cycles, weight values per test, data acquisition process, sensors used, and temperature correction approach. The only difference was the timing, as the second test session occurred a week after the first. This interval introduced changes in laboratory environmental conditions.

The results of this second session were compared to those from the first, focusing exclusively on data corrected for temperature. The comparison, as shown in the accompanying figures, revealed discrepancies between the two datasets. The observed shift was significant and could not be attributed to disturbances or procedural errors. The hypothesis of an incorrect thermal constant was dismissed since altering this constant within a reasonable range only increased data dispersion without aligning the datasets. The only remaining unexamined factor was humidity, whose data trend had been recorded during all tests. This variable was deemed the most plausible explanation for the data shift. Since both sessions followed identical procedures, the only differing factor was environmental conditions. With temperature already accounted for, humidity emerged as the primary suspect. This hypothesis was further supported by the hygroscopic nature of PLA, the gearbox material, which could undergo structural deformation even with minor changes in humidity. Unlike temperature, a controlled characterization test for humidity was not feasible due to the stringent requirements of maintaining stable humidity over extended periods, which only a climatic chamber could achieve. Given that disassembling the gearbox from the bench would compromise the experimental setup, a numerical approach was adopted to determine the humidity constant. The method involved a parametric analysis of the humidity factor, conducted alongside the linear fit for determining the torque coefficient. The final humidity coefficient was determined by minimizing the normalized residuals of the data fit for various coefficient values. This dual analysis yielded both the humidity and torque coefficients. To simplify the explanation, the logical steps followed in this analysis are illustrated in Figure 93. The humidity correction phase mirrored the structure of the temperature correction. The wavelength data were adjusted to a zero-humidity condition, adding an additional term to the previous correction formula:

$$\lambda i{-}corrected = \lambda i{-}test - Ti{-}test\ KT - Hi{-}test\ KH \tag{4}$$

This comprehensive correction approach addressed both thermal and humidity influences on the wavelength data.
To make this process enough accurate, an additional data set is generated. To keep the data consistent, the same procedure is maintained, and again the data acquisition took place on a separate day from the previous tests. In this way, the numerical analysis is carried out with a database subjected to three different environmental conditions.

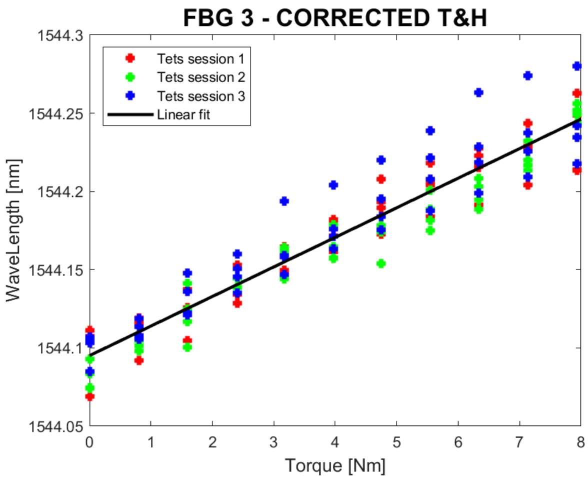

Figure 12 Data corrected and linear fit.

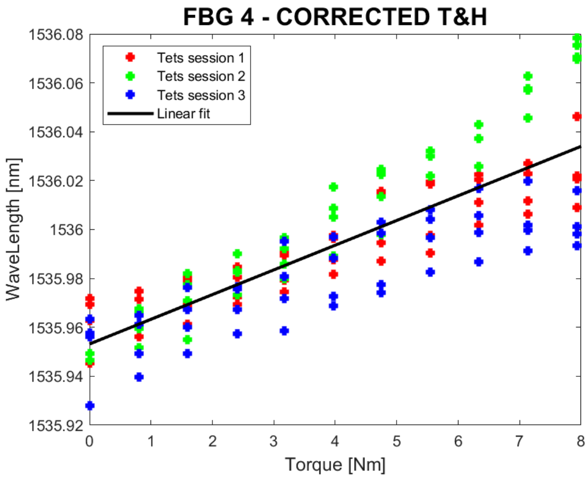

Figure 13 Data corrected and linear fit.

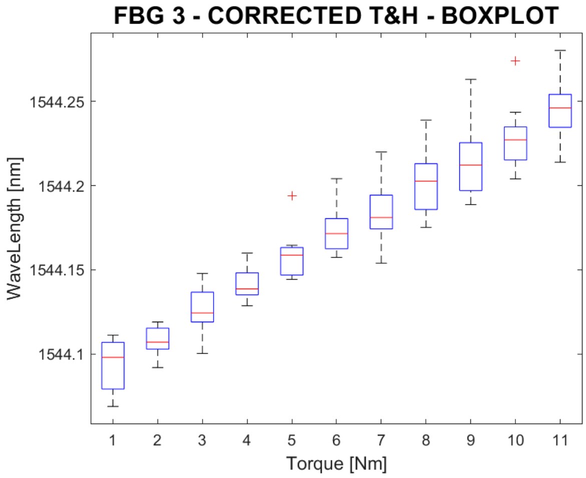

Figure 14 Boxplot of experimental data.

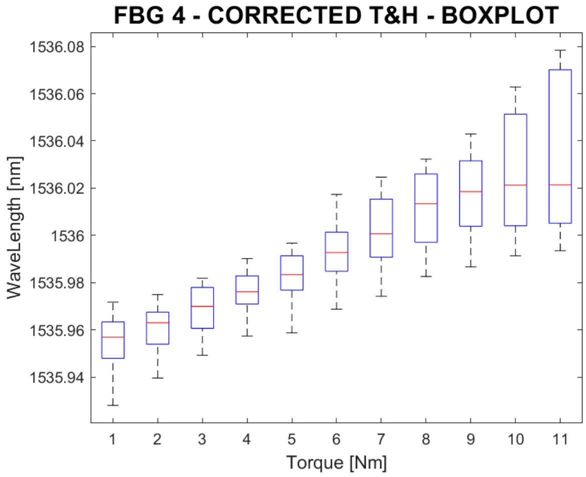

Figure 15 Boxplot of experimental data.

Once the analysis is completed, the following results are obtained. Since this is a linear fit, in addition to the KQ value representing the angular coefficient, constant terms were also derived for the respective sensors. Below are reported the graphs showing the original unadjusted data and the fully corrected data by applying the KH and KT coefficients from the previous tables. The line of the interpolating fit's also superimposed on the latter graphs.

6 CONCLUSIONS

At the conclusion of all experimental and analytical procedures, several key results were obtained on the topics investigated. The performance of FBG sensors proved highly impressive for system monitoring, particularly in terms of the speed and sensitivity offered by this sensor type. However, like any other component, the FBG sensor requires a tailored installation process involving specific support elements depending on its intended application. In this study, the material properties of the components where the sensors were installed significantly altered the characteristic coefficients previously deemed valid. To employ FBGs as torque sensors, it was necessary to develop a corrective method to account for variations in temperature and humidity. Unfortunately, while tests were performed to characterize the temperature factor, humidity issues could only be addressed numerically. The results in this area were not entirely satisfactory. Of the four sensors installed, only one provided data suitable for determining the torque applied to the system, and this was accompanied by a substantial and unstable error in the final calculated values. Consequently, this solution did not resolve the issues observed during the preliminary phase of the study, in which the torque data acquired from the test bench were often inconsistent. Despite these challenges, the improved performance of FBG 3 indicates that better results could potentially be achieved with higher-quality test bench components. For more precise investigations, it would be necessary to conduct tests on a system with a structure closely resembling the final design, or at least one that avoids the use of plastic components, as these were shown to introduce considerable uncertainty and noise into the data. Additionally, given the demonstrated influence of environmental conditions and installation methods, the component on which the FBG sensors are mounted must undergo a dedicated calibration process to determine the characteristic coefficients of the phenomena being measured. If these precautions validate the feasibility of measuring the torque load experienced by an EMA, the acquired data could be leveraged not only for monitoring purposes but also as input for simulation models. Moreover, if the FBG-based torque measurement method proves sufficiently reliable, the data could even be incorporated into a feedback loop within an EMA's position control system. Considering these possibilities, along with the demonstrated thermal capabilities and the numerous inherent advantages of fiber-optic technology, FBG sensors can be reasonably regarded as a promising solution for integration into innovative aerospace monitoring systems.

AKNOWLEDGEMNTS

Authors sincerely thanks dott. Paolo Girardi, dott. Michele Drivio and dott. Francesco Gerbino for their precious work conducted during their master thesis work. Their passion, professionalism and dedication to work were an essential element for the success of this work.
The authors would also like to thank the PhotoNext interdepartmental research center of the Polytechnic of Turin for its support in providing instrumentation for optical measurement technologies.

REFERENCES

[1] M. J. Cronin, All-electric vs conventional aircraft - The production/operational aspects. *Journal of Aircraft*, vol. 20, no. 6, pp. 481–486, May 2012.

[2] M. Howse, All electric aircraft. *IEE Power Engineer*, vol. 17, no. 4, pp. 35–37, 2003.

[3] R. E. Quigley, More Electric Aircraft. *Proceedings Eighth Annual Applied Power Electronics Conference and Exposition*, pp. 906–911, 1993.

[4] A. Weimer, The Role of Electric Machines and Drives in the More Electric Aircraft. *Electric Machines and Drives Conference*, IEEE International, Volume: 1, 2003.

[5] Y. Deng, S. Y. Foo, and I. Bhattacharya, Regenerative electric power for More Electric Aircraft. *IEEE SOUTHEASTCON 2014,* Nov. 2014.

[6] Z. Yin, N. Hu, J. Chen, Y. Yang, and G. Shen, A review of fault diagnosis, prognosis and health management for aircraft electromechanical actuators. *IET Electric Power Applications*, vol. 16, no. 11, pp. 1249–1272, Nov. 2022.

[7] M. H. Taha. *Power Electronics Application for More Electric Aircraft*, InTech, 2012.

[8] A. G. Garriga, S. S. Ponnusamy, and L. Mainini, A multifidelity framework to support the design of more-electric actuation. *2018 Multidisciplinary Analysis and Optimization Conference*, 2018.

[9] W. Wu, Y. R. Lin, L. C. Chow, E. Gyasi, J. P. Kizito, and Q. H. Leland, Electromechanical actuator fan failure analysis and safety-critical design. *IEEE Aerospace and Electronic Systems Magazine*, vol. 32, 2017.

[10] C. Wang, I.-S. Fan, and S. King, Failures Mapping for Aircraft Electrical Actuation System Health Management. *Proceedings of PHM Society European Conference, 2022.*

[11] T. Missala, Electromechanical actuators – Selected safety-related problems. *Advances in Intelligent Systems and Computing*, vol. 267, pp. 175–186, 2014.

[12] M. Azam, S. Ghoshal, D. Taylor, T. Chirico, and E. Gregory, Prognostics and Health Management (PHM) of Electromechanical Actuation (EMA) systems for next-generation aircraft. *Proceedings of AIAA Infotech at Aerospace (I at A) Conference, 2013*.

[13] V. Madonna et al., Thermal Overload and Insulation Aging of Short Duty Cycle, Aerospace Motors. *IEEE TRANSACTIONS ON INDUSTRIAL ELECTRONICS*, vol. 67, no. 4, 2020.

[14] J. Zhou et al., High-ampacity conductive polymer microfibers as fast response wearable heaters and electromechanical actuators, *Journal of Material Chemistry C*, vol. 4, no. 6, pp. 1238–1249, 2016.

[15] P. C. Berri, M. D. L. Dalla Vedova, A. Aimasso, C. G. Ferro, P. Maggiore, and G. Riva, 3D PRINTING TO SUPPORT EXPERIMENTAL ACTIVITIES:

LESSONS LEARNED FROM RAPID PROTOTYPING OF AN ELECTROMECHANICAL ACTUATOR GEARBOX. *International Journal of Mechanics and Control*, vol. 24, no. 1, 2023.

[16] A. Aimasso, P. C. Berri, and M. D. L. Dalla Vedova, A genetic-based prognostic method for aerospace electromechanical actuators. *International Journal of Mechanics and Control*, vol. 22, no. 2, 2021.

[17] A. Aimasso, L. Baldo, M. D. Vedova, and P. Maggiore, PROGNOSTICS OF AEROSPACE ELECTROMECHANICAL ACTUATORS USING THE FAILURE MAPS TECHNIQUE. *International Journal of Mechanics and Control*, vol. 23, no. 1, 2022.

[18] Safa. Kasap. *Optoelectronics and photonics : principles and practices*, Prentice Hall, 2001.

[19] S. J. Mihailov, Fiber Bragg Grating Sensors for Harsh Environments. *Sensors*, vol. 12, pp. 1898–1918, 2012.

[20] A. Behbahani, M. Pakmehr, and W. A. Stange, Optical Communications and Sensing for Avionics. *Springer Handbooks*, Springer Science and Business Media Deutschland GmbH, 2020, pp. 1125–1150.

[21] S. J. Mihailov et al., Ultrafast laser processing of optical fibers for sensing applications. *Sensors*, Feb. 02, 2021, MDPI AG.

[22] S. J. Mihailov et al., Extreme Environment Sensing Using Femtosecond Laser-Inscribed Fiber Bragg Gratings. Optics Express, 2022.

[23] M. D. L. Dalla Vedova, P. C. Berri, and A. Aimasso, Environmental sensitivity of Fiber Bragg Grating sensors for aerospace prognostics. *Proceedings of the 31st European Safety and Reliability Conference, ESREL 2021*, 2021